

A Nondestructive and Position-Unrestricted Integrated Photonic Chip Detection Method

JINZE SHI, CHANGYING LI, JIAJUN WAN AND XIAOPING LIU*

School of Physical Science and Technology, ShanghaiTech University, Shanghai 201210, China

**liuxp1@shanghaitech.edu.cn*

Abstract: As the number and diversity of devices integrated into photonics on-chip systems continue to escalate, it becomes increasingly challenging to determine the modes' behavior on specific positions of concern relying solely on preprocessed couplers. Interference of two coherent pump beams has the capability to induce a periodic carrier distribution in the material, thus modulating the refractive index and effectively creating a diffraction grating. In this study, a nondestructive and position-unrestricted detection method based on a carrier grating is proposed. We develop a theoretical model to calculate carrier dynamics under various pump configurations. Leveraging the Finite-Difference Time-Domain (FDTD) method and accounting for Free Carrier Index (FCI) and Free Carrier Absorption (FCA) effects, meticulous analysis of the quantitative impact of pump intensity and radius on the diffraction efficiency of the carrier grating and its far-field divergence characteristics are provided. Ultimately, this research contributes to a discussion on the feasibility of high spatial-resolution experimental approaches.

1. INTRODUCTION

The compatibility of integrated photonics with COMOS processes has led to rapid advancements in the field, offering significant potential applications in areas such as sensing [1, 2] and computing [3]. However, as on-chip device scale and system complexity continue to grow, drawbacks such as processing deviations and long fabrication cycles not only burden the design and iteration of on-chip systems [4] but also increase the difficulty of detecting the mode propagation characteristics at a specific location. Traditional on-chip system detection methods rely on input and output information. For instance, in photonics computing systems, the system's normal operation can be inferred from the output signal given a specific input. In this context, the system can be likened to a black box within a circuit, the primary objective of this work is to present a "voltmeter for optics," a nondestructive method for measuring the optical field at any arbitrary position within a photonic chip system.

The input and output of integrated photonics chips typically require connections to free space or optical fibers, with coupler being the most commonly used means. Depending on their location, a coupler can be categorized as edge coupler [5] and grating coupler [6]. In cases where high bandwidth requirements are not necessary, grating couplers are often more suitable due to their flexible fabrication positions. Grating couples are based on altering wave vectors through grating, where a specific fabrication period can achieve coupling in or out along a specific direction [6]. In its essence, grating involves materials with periodic variations in refractive index, which can be achieved not only through alternating materials but also through the periodic distribution of physical fields within the same material, such as temperature, stress, carrier concentration, etc. Therefore, generating a grating by introducing a periodic variation of a physical field is a way to achieve detection at arbitrary on-chip positions. This technique is generally called Transient Grating Spectroscopy (TGS) [7–9]. TGS employs two coherent pulsed pump beams to generate an interference pattern on the sample surface, as shown in Fig. 1 (a). This interference pattern results in a periodic distribution of the physical field. By adjusting the delay τ of the probing light (Fig. 1 (b)), dynamic processes like carrier transport can be characterized. Spatially periodic optical field can induce a spatially periodic carrier concentration, and according to the Free Carrier Index (FCI) and Free Carrier Absorption (FCA) effects [10], the material's dielectric

47 coefficient also periodically changes in space, leading to the grating effect known as a carrier
48 grating.

49 For bulk materials, research utilized pump light with wavelengths greater than the silicon
50 bandgap (1.1 eV) to create a carrier grating in bulk silicon material and used this grating to measure
51 carrier lifetimes [11]. In the SOI (Silicon-on-Insulator) system, research has explored the off-chip
52 reconfigurable analysis of integrated devices using pump light and a Spatial Light Modulator
53 (SLM) [12–14]. Additionally, studies have employed pump-probe techniques to measure dynamic
54 processes such as single-photon absorption (SPA), and two-photon absorption (TPA) [15, 16],
55 Auger recombination, and surface recombination [17, 18] in waveguides. However, there is
56 currently no research on characterizing integrated photonics systems or device performance using
57 TGS. The carrier grating's efficiency in coupling-out propagation modes or, in other words, its
58 diffraction efficiency (the ratio of diffracted intensity to incident intensity [19]) for waveguides
59 requires critical quantitative analysis. Besides, to construct an experiment, far-field analysis
60 including divergence and direction is necessary to investigate. Section 3 primarily discusses the
61 preconditions involved in this work's feasibility, including wave vector analysis, plasma effect,
62 and damage threshold. Section 4 conducts theoretical analysis on carrier dynamics within SOI
63 frame under pump interference. Section 5 utilizes the FDTD method to stimulate diffraction
64 efficiency and far-field analysis under different refractive index maps. Section 6 presents an
65 analysis and discussion of experimental configurations, and finally, the conclusion is provided in
66 the last section.

67 2. PRECONDITIONS

68 2.1. Wave Vector Analysis

69 As shown in Fig. 1(a), two coherent pump beams generate interference fringes on the sample
70 surface with a fixed period Λ . The relationship between the fringe period and the angle ϕ of the
71 pump beams is given by:

$$|\vec{k}_1| \sin(\phi) + |\vec{k}_2| \sin(\phi) = 2\pi/\Lambda \quad (1)$$
$$|\vec{k}_1| = |\vec{k}_2| = \frac{2\pi n_{cladding}}{\lambda_{pump}}$$

72 For a fixed wavevector of the probe light, changing the grating's period can alter the direction
73 of its diffraction signal. A similar analysis can be applied to the SOI architecture, taking a strip
74 waveguide as an example, as illustrated in Fig. 1(c). The probe light represents a propagating
75 mode within the waveguide. The wavevector of the first-order diffracted light must satisfy the
76 phase-matching condition, as depicted in Fig. 1(d), which can be expressed as:

$$|\vec{k}_3| - K = |\vec{k}_4| \sin(\theta) \quad (2)$$
$$|\vec{k}_3| = 2\pi n_{eff}/\lambda_{probe}$$
$$|\vec{k}_4| = 2\pi n_{cladding}/\lambda_{probe}$$

77 Here, n_{eff} represents the effective refractive index of the propagating mode within the
78 waveguide, and $n_{cladding}$ is the refractive index of the waveguide's cladding. To ensure the
79 presence of diffracted light, the grating period must satisfy $K < 2|\vec{k}_3|$. Otherwise, the grating
80 period would fall into the range of Subwavelength Grating (SWG) structures and would not serve
81 as a diffraction grating. To avoid multiple diffraction orders and energy losses caused by oblique
82 incidence at the cladding-air interface, making the diffraction signal emerge perpendicularly, i.e.,
83 $\theta = 0$, is a suitable choice.

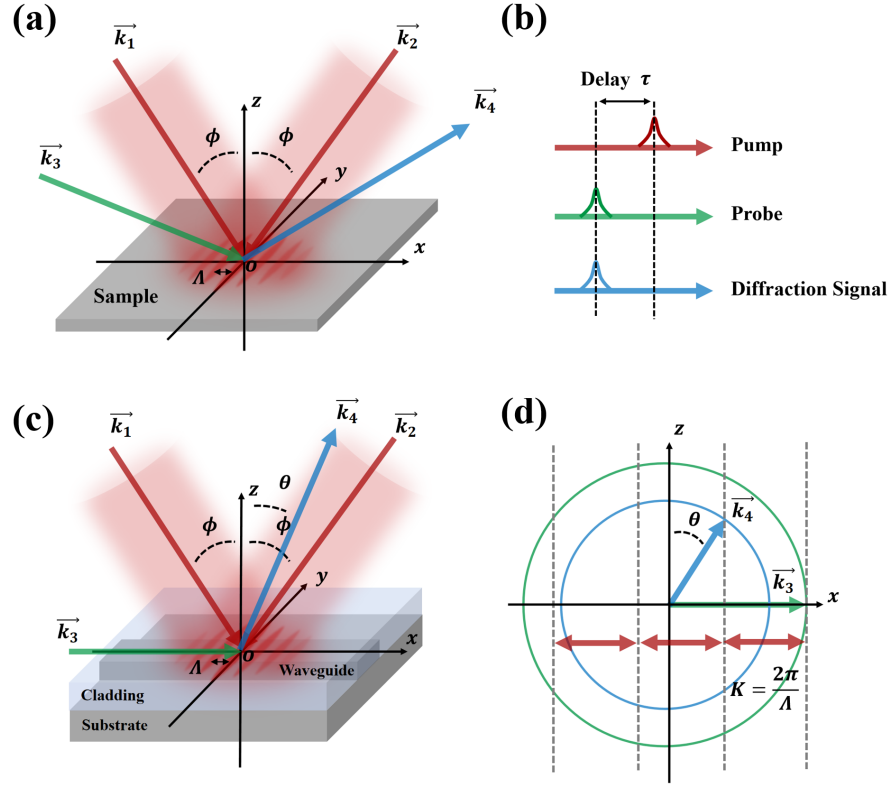


Fig. 1. (a) Schematic diagram illustrating the wavevector relationships in TGS. \vec{k}_1 , \vec{k}_2 , \vec{k}_3 , and \vec{k}_4 represent the wavevectors of the two pump beams, the probe light, and the diffracted signal, respectively. (b) Diagram depicting the time-delay relationships between the pump beams, probe light, and diffracted light. (c) Schematic illustration of the wavevector relationships in the TGS setup for the SOI system. (d) Phase-matching relationships for different types of wavevectors.

84 2.2. Plasma Effect

85 The plasma effect, also known as the plasma dispersion effect or plasma resonance effect, is a
 86 phenomenon where free carriers in a material interact with electromagnetic waves, resulting
 87 in changes in the material's real part of the refractive index: Free Carrier Index (FCI) and
 88 imaginary part of the refractive index: Free Carrier Absorption (FCA). Theoretically, quantitative
 89 relationships can be derived through various models [20, 21] to describe these effects. However,
 90 in practical applications, empirical formulas based on experimental observations are often used
 91 to describe the relationships between FCI, FCA, and carrier concentrations [10].

$$\begin{aligned} \tilde{n} &= n + ik \\ \Delta n &= -[8.8 \times 10^{-4} N_e + 8.5(N_h)^{0.8}] \times 10^{-18} \\ \Delta k &= \frac{\lambda}{4\pi} [8.5N_e + 6.0N_h] \times 10^{-18} \end{aligned} \quad (3)$$

92 N_e and N_h (cm^{-3}) represent the concentrations of electrons and holes, respectively. Fig.
 93 2 depicts the relationship between the absolute values of the real and imaginary parts of the
 94 refractive index and the concentrations of both types of carriers. It's only when the concentration

approaches 10^{20} cm^{-3} that there is a 0.1 magnitude change in the refractive index, indicating that to enhance the coupling efficiency of the grating, it is necessary to increase the intensity of the pump light intensity ($\text{W} \cdot \mu\text{m}^{-2}$) to generate more carriers per unit time. However, this introduces a new issue: will increasing the laser intensity potentially damage (e.g., burn holes or melt) the on-chip system and devices?

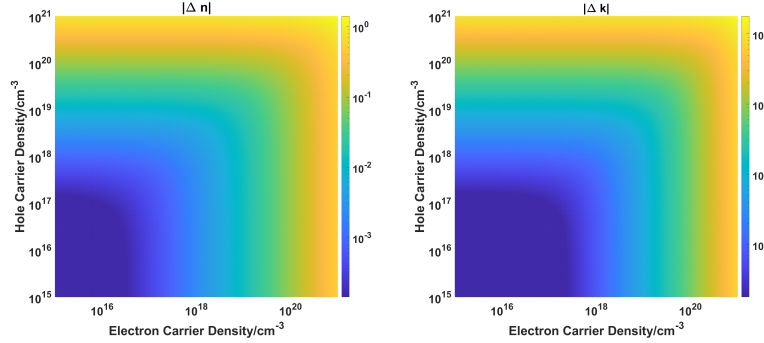


Fig. 2. Change in absolute values of refractive index real and image parts induced by free Electrons and Holes concentration.

2.3. Damage Threshold

The damage threshold is defined as the upper limit of laser intensity to prevent the chip from being damaged. Its physical meaning is the laser power per area. For pulsed pump light, whose power varies with time and space, the damage threshold corresponds to the peak light intensity of each pump pulse. When the laser energy density is too high, it can lead to a situation where the rate of carrier generation exceeds the relaxation rate, resulting in heat accumulation that raises the temperature of the chip material. If the temperature exceeds the melting point, the chip can be damaged. For different pulse durations, different physical processes involving relaxation come into play, and the order of magnitude of the damage threshold varies accordingly. For example, with a pulse duration of 10 ps (i.e., intensity reduces to $1/e^2$ at 5 ps from the peak time), the main processes involved are carrier generation and recombination. At the 10 ns level, carrier diffusion also plays a role, and at 10 ms or continuous light levels, thermal diffusion becomes significant. Reducing the pulse duration significantly increases the order of magnitude of the damage threshold. For silicon material pumped by a laser wavelength of 1064 NM as an example, the damage threshold for a 10 ps pulse is $823.93 \text{ W} \cdot \mu\text{m}^{-2}$, and for a 10 ns pulse, it is $5.64 \text{ W} \cdot \mu\text{m}^{-2}$ [22]. From nanosecond to picosecond pulsed laser, decreasing the time scale by three orders of magnitude results in an increase of two orders of magnitude in the damage threshold. Although smaller time scales lead to higher damage thresholds, they also require stricter experimental time precision. To provide a more comprehensive analysis of experimental feasibility, this discussion will also consider cases with relatively larger pulse durations. To ensure that the chip is not damaged, the modeling discussed below will set the pulse pump light intensity to be lower than the damage threshold.

3. CARRIER DYNAMICS ANALYSIS

3.1. interference Generation

As shown in the illustration of Fig. 1(c), for two coherent Gaussian pump beams with equal radius a and peak intensity I_0 , considering the interface reflectivity R , the interference optical intensity in the x direction can be deduced as:

$$I(x, t) = 2I_0(1 - R)e^{[-x^2 \cos(\phi)^2/a^2]}[1 + \cos(\frac{2\pi}{\Lambda}x)]e^{-(t-t_0)^2/\tau^2} \quad (4)$$

127 Where t_0 and τ are the time at which the peak of the pump light occurs and the pulse's time
 128 width, respectively. The interference fringe period Λ is set to ensure that the diffracted light exits
 129 the waveguide surface perpendicularly, i.e., $K = |\vec{k}_4| \rightarrow \Lambda = \lambda/n_{eff}$. Since the interference
 130 fringe period is fixed, changes in the detection spatial resolution - the radius $r_0 = a/\cos(\phi)$ of the
 131 carrier grating - will influence the number of fringes at a detection point, which not only affects
 132 the diffraction efficiency of the grating but also influences the divergence characteristics of the
 133 diffracted light. Concerning diffraction, only the intensity distribution with periodic variations
 134 affects the coupling, while the non-periodic part only introduces undirected scattering [23].
 135 Therefore, it is necessary to define a variable which could represent the variation of the periodic
 136 portion of the pump $I(x)$. As Eq. (4) shown, $I(x)$ can be treated as a Gaussian-shaped DC signal
 137 supposed with another Gaussian-shaped AC signal. The range of this AC part, defined as Δ which
 138 equals to $4I_0(1 - R)$ in Eq. (7), accounts a significant matter in grating. Studying the evolution
 139 of the range Δ of the periodic parts of carriers concentration over time is crucial for analyzing the
 140 diffraction efficiency of the carrier grating. This will be discussed in detail in the following parts.

141 3.2. Carrier Dynamics

142 The generation and recombination of carriers involve various nonlinear physical processes.
 143 Silicon material has a bandgap of 1.12 eV, which means that light with wavelengths shorter
 144 than 1070 nm can excite valence band electrons into the conduction band, thereby generating
 145 free carriers (electrons and holes). The two primary mechanisms for the generation of free
 146 carriers under the influence of the pump light are single-photon absorption (SPA) and two-
 147 photon absorption (TPA). Higher-order nonlinear processes require higher optical intensities
 148 for pumping. In bulk materials, the recombination of free carriers from the conduction band
 149 to the valence band mainly occurs through Auger recombination and radiative recombination.
 150 Auger recombination becomes significant typically at carrier concentrations on the order of
 151 10^{19} cm^{-3} or higher, which is necessary for the configuration studied in this paper. Defective
 152 semiconductors introduce energy states between the conduction and valence bands, leading
 153 to Shockley-Read-Hall (SRH) recombination. Defect states near the material's surface can
 154 also lead to surface recombination. However, the effective range of surface recombination for
 155 silicon and silicon dioxide is approximately 50 nm from the surface [24]. In the discussion
 156 below, we will focus on a 1 μm wide waveguide as the research subject and temporarily neglect
 157 SRH recombination and surface recombination. Therefore, the evolution of electron and hole
 158 concentrations over time can be described as follows:

$$\frac{\partial N(x, t)}{\partial t} = \alpha(1 - R)I(x, t)/hv + \beta(1 - R)I(x, t)^2/2hv + D_n \frac{\partial^2 N(x, t)}{\partial x^2} \quad (5)$$

$$-C_n[N(x, t)^2 P(x, t) - n_0^2 p_0] - C_p[N(x, t)P(x, t)^2 - n_0 p_0^2] - B[N(x, t)P(x, t) - n_0 p_0]$$

$$\frac{\partial P(x, t)}{\partial t} = \alpha(1 - R)I(x, t)/hv + \beta(1 - R)I(x, t)^2/2hv + D_p \frac{\partial^2 P(x, t)}{\partial x^2} \quad (6)$$

$$-C_n[N(x, t)^2 P(x, t) - n_0^2 p_0] - C_p[N(x, t)P(x, t)^2 - n_0 p_0^2] - B[N(x, t)P(x, t) - n_0 p_0]$$

159 In the above equation, $N(x, t)$ and $P(x, t)$ are functions of electron and hole concentrations
 160 with respect to position and time. α and β represent the SPA and TPA coefficients, hv is the
 161 energy of a single photon. C_n , C_p , and B are the coefficients for Auger recombination and direct

162 recombination, D_n and D_p are the bipolar diffusion coefficients for electrons and holes, and n_0
 163 and p_0 are the intrinsic semiconductor electron and hole concentrations, respectively.

164 The optical field generated by the pump light interference has only a component along the z
 165 direction. Taking the SOI framework as the subject of study, the optical field reflects at the surface
 166 of the cladding waveguide, resulting in energy loss, which is accounted for by the constant R . For
 167 commonly used pump light with a wavelength of 800 nm, the silicon material has an absorption
 168 depth of approximately 80 μm , which is much greater than the typical waveguide thickness of
 169 220 nm to 340 nm. Additionally, compared to the x direction, the intensity distribution in the y
 170 direction changes slowly. Therefore, it is assumed that the intensity is sufficiently uniform in
 171 both the z and y directions, allowing for the neglect of carrier diffusion in these two dimensions.
 172 As mentioned earlier, only the periodic part of the optical intensity has the effect of a grating.
 173 Carrier diffusion in the x direction significantly affects the duration of the periodic part.

174 3.3. Numerical Calculation Results

175 This subsection discusses the numerical calculation results of the above theoretical model using
 176 The FTCS (Forward in Time, Central in Space) Explicit Method. Substituting the specific
 177 parameters listed in Table 1 allows for numerical calculations of the spatial distribution of
 178 carrier density evolving over time. The boundary condition is set as the gradient of the carrier
 179 concentration equals to zero at the boundary ($x = \pm 30\mu m$). To ensure the convergence of the
 180 results, the stability condition $\delta t < \delta^2 x / 2D_n$ is required.

Coefficient	Physical Meaning	Value
α	SPA Coefficient @800nm	$8.5 \times 10^2 cm^{-1}$
β	TPA Coefficient @800nm	$1.0 \times 10^{-14} cm \cdot W^{-1}$
C_n	Auger Recombination Coefficient	$1.1 \times 10^{-30} cm^6 \cdot s^{-1}$
C_p	Auger Recombination Coefficient	$0.3 \times 10^{-30} cm^6 \cdot s^{-1}$
B	Radiative Recombination Coefficient	$1.1 \times 10^{-14} cm^{-3} \cdot s^{-1}$
n_0, p_0	Intrinsic Carrier Concentration Coefficient	$1.0 \times 10^{10} cm^{-3}$
D_n	Electrons Diffusion Coefficient	$5.0 cm^2 \cdot s^{-1}$
D_p	Holes Diffusion Coefficient	$1.7 cm^2 \cdot s^{-1}$

Table 1. Numerical calculation parameters.

181 In the scenario with a pulse width of 10 ps, the evolution of pump intensity distribution $I(x, t)$,
 182 electron concentration distribution $N(x, t)$, and hole concentration distribution $P(x, t)$ over time
 183 is depicted in Fig. 3(a), 4(b), and 4(c), respectively. The spatial periodic distribution of the
 184 pump light induces a similar spatial distribution of carriers. The range of the periodic part of
 185 $N(x, t)$ and $P(x, t)$ are illustrated as Δ_N and Δ_P in Fig.3 (d), which provides 9 time snapshots
 186 of the simulation process for both carriers from 10 ps to 90 ps. Due to carrier diffusion, they
 187 manifest a decay and Δ_N exhibit a faster decay compared to holes. Considering the device should
 188 not be damaged, the magnitude of the pump light intensity in this simulation is about 2 orders
 189 of magnitude below the damage threshold (283.54 $W \cdot um^{-2}$ @ 10ps, 800nm), and the Auger
 190 recombination effect is not prominent. The direct radiative recombination lifetime is much longer

191 compared to the Δ decay process, so there is no significant change in the non-periodic part within
 192 the computed time range.

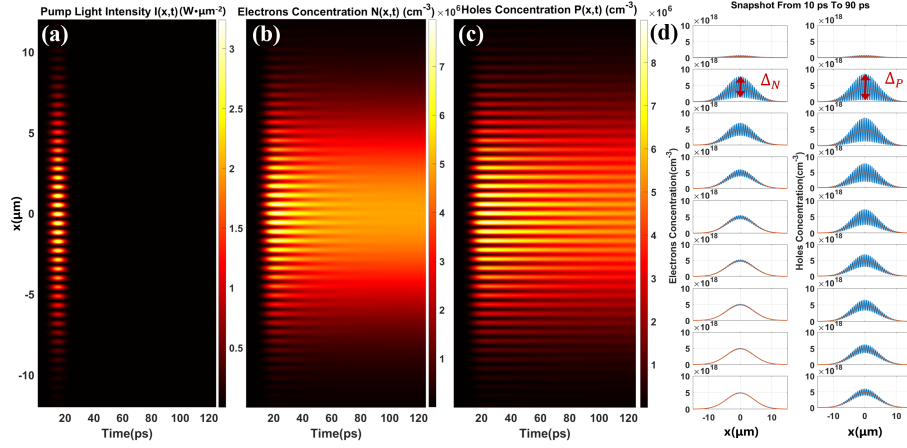


Fig. 3. **F(a)**Evolution of the interfered optical field distribution at the waveguide surface over time: $I(x, t)$, with a pulse width set to 10 ps and I_0 set to $1 \text{ W} \cdot \mu\text{m}^{-2}$. **(b)**Evolution of the electron concentration distribution over time: $N(x, t)$. **(c)**Evolution of the hole concentration distribution over time: $P(x, t)$. **(d)**Time snapshots of the concentration distribution for both types of carriers from the calculated results in (b) and (c). The red line in the figures represents the move mean of $N(x, t)$ and $P(x, t)$. Δ_P and Δ_N are the range of periodic parts as illustrated, which equals the range of the origin signal minus the move mean signal.

193 The process of Δ evolving is plotted in Fig. 4 for three different pump modes (10 ps , 10
 194 ns , CW). The power for all three pump modes is set to be about one order of magnitude
 195 below the damage threshold. For the 10 ps pump pulse, the peak carrier concentration reaches
 196 approximately 10^{20} cm^{-3} . Because the pump pulse width is much smaller than the time scale of
 197 diffusion, carrier generation occurs faster than diffusion, and both carriers' Δ peaks are close to
 198 each other and lag behind the pump peak in time. However, the lifetime of Δ_P is longer than that
 199 of electrons. This lifetime can be roughly estimated as $\tau_{\Delta_P} \approx (\Lambda/2)^2/D_P \approx 53.25 \text{ ps}$, which is
 200 comprehended as the time needed for a hole move from one peak of $P(x)$ to the nearest valley
 201 and it is as the same order of the numerical calculation. Compared to the lifetime of Δ_N , after
 202 the pump pulse ends, changes in refractive index are primarily caused by holes.

203 For the 10 ns pump pulse, the diffusion effect becomes prominent within the pump duration,
 204 and both carrier concentration peaks reach the order of 10^{18} cm^{-3} with nearly identical durations.
 205 Δ_N is one-third of that for holes, corresponding to the difference in their diffusion coefficients. In
 206 the case of CW pumping, Δ_N reaches equilibrium at about 100 ps , while Δ_P stabilizes in about
 207 300 ps . The stabilized concentration for holes is approximately three times that of electrons,
 208 which corresponds to their respective diffusion coefficients. The peak values are on the order of
 209 10^{15} cm^{-3} .

210 In summary, using a shorter pump pulse width allows testing at higher pump intensity in
 211 experiments. In this case, the refractive index changes significantly, leading to higher diffraction
 212 efficiency. However, this state only lasts for about 50 ps . The advantage of using continuous light
 213 as a pump is that the grating remains present continuously. However, the induced refractive index
 214 change is too low, and the diffraction light intensity may be submerged in waveguide scattering
 215 or other noises. Specific feasible experimental methods are discussed in the sixth section. In the
 216 next section, the impact of pump peak intensity and grating radius on diffraction efficiency and

217 far-field distribution will be analyzed using FDTD simulations for different refractive index maps.

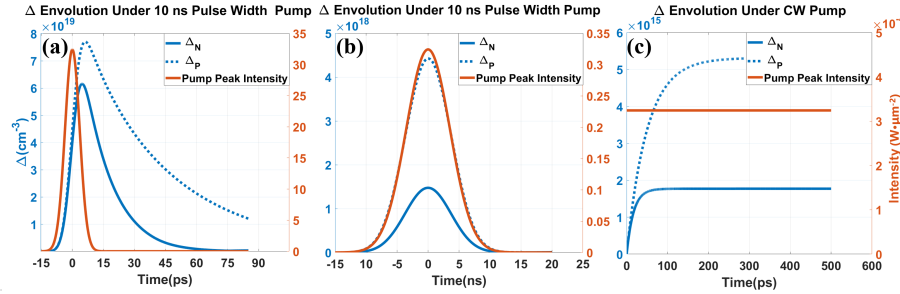


Fig. 4. (a) Evolution of the maximum of the interfered optical field, the Gaussian periodic parts' range of electron spatial concentration and hole spatial concentration Δ_N and Δ_P , for a pulse width of 10 ps with $I_0 = 10 \text{ W} \cdot \mu\text{m}^{-2}$. (b) Case of a pulse width of 10 ns with $I_0 = 0.1 \text{ W} \cdot \mu\text{m}^{-2}$. (c) Case of continuous-wave pump light, $I_0 = 0.0001 \text{ W} \cdot \mu\text{m}^{-2}$.

218 4. FDTD SIMULATION

219 4.1. Diffraction Efficiency

220 Diffraction efficiency is a crucial metric for assessing the capabilities of carrier gratings, and its
 221 quantitative calculation can be traced back to the diffraction formula for ultrasonic waves [25],
 222 which excite periodic stress distributions within materials, thereby generating sinusoidal refractive
 223 index modulations. The first-order diffraction efficiency for this grating can be expressed as
 224 $\eta = \frac{I_1}{I_0} = |J_1[\frac{2\pi d(\Delta n + i\Delta k)}{\lambda}]|^2$. Where I_0 and I_1 represent the intensities of the incident and
 225 first-order diffracted light, respectively, and d denotes the penetration depth of ultrasound in the
 226 material. J_1 is the first-order Bessel function. Subsequent literature also suggests [11, 26] that,
 227 when the change in refractive index is small or the grating thickness is low, the Bessel function
 228 can be approximated as a quadratic function $\eta \propto |\Delta n + i\Delta k|^2$

229 In the context discussed in this paper, the aforementioned equations are not applicable. This
 230 is because, considering the influence of the grating dimensions, the number of stripes is not
 231 sufficient to approximate them as a sinusoidal grating. Furthermore, in the SOI system, incident
 232 light does not originate from free space and impinge directly onto the grating; rather, it passes
 233 through the waveguide structure before encountering the grating. Due to free carrier absorption,
 234 its intensity undergoes non-uniform attenuation along the propagation direction, influenced by
 235 the free carrier absorption. Therefore, providing a quantitative analysis of diffraction efficiency
 236 within the SOI framework is a complex mathematical process. Numerical calculations using the
 237 Finite-Difference Time-Domain (FDTD) method can offer a more efficient means of obtaining
 238 extensive data in this SOI context.

239 4.2. Simulation Settings

240 In light of the preceding analysis, the evolution of carrier concentration distributions $N(r, t)$ and
 241 $P(r, t)$ can be computed by Eq. (5)-(6). These distributions can be transformed into the refractive
 242 index distribution at each moment $\tilde{n}(r, t) = n(r, t) + ik(r, t)$ using Eq. (3). This distribution
 243 corresponds to a diffraction efficiency $\eta(t)$. For different moments in time when $\tilde{n}(r, t)$ varies,
 244 the diffraction efficiency η_{max} corresponding to the moment when the range of periodic part of
 245 $|\tilde{n}|$ is maximum, denoted as $\Delta|\tilde{n}|_{max}$, is the most significant. Calculating η_{max} allows for the
 246 most efficient analysis of the impact of various pump parameter settings.

247 The simulation section of this study considers $60 \mu\text{m}$ long, $1 \mu\text{m}$ wide, and 220 nm thick SOI
 248 waveguide. A 1550 nm fundamental mode is chosen as the input at one end of the waveguide, as
 249 shown in Fig. 5(a). In the y direction, the grid resolution is $0.1 \mu\text{m}$, while in the z direction, it is
 250 $0.02 \mu\text{m}$. Under this level of mesh precision, the effective refractive index of the propagating
 251 mode falls within the convergence range. The grid resolution in the x direction has been
 252 adjusted to one-fifteenth of the grating period $0.5647 \mu\text{m}$, approximately $0.0376 \mu\text{m}$, which
 253 satisfies the phase match condition for vertical emission. The peak pump intensities I_0 are set
 254 to $1, 2, 4, 6, 8, 10, 20, 40, 60, 80, 100 \text{ W} \cdot \mu\text{m}^{-2}$, with a pulse width of 10 ps . To ensure a large
 255 sweep of parameters, the last set of pump peak intensity generates an interference intensity
 256 distribution whose maximum reaches the damage threshold. Considering the choice of detection
 257 spatial resolution, for each intensity, the grating radius r_0 is taken as $1, 2, 4, 6, 8, 10 \mu\text{m}$. The
 258 refractive index distribution $\tilde{n}(r)$ corresponding to $\Delta|\tilde{n}|_{max}$ is obtained numerically by Matlab
 259 for different sets of parameters. The import(n,k) function in the Lumerical FDTD module is used
 260 to import this refractive index distribution. All refractive index distributions are set within a
 261 region centered at $x = 0 \mu\text{m}$ and spanning $\pm 30 \mu\text{m}$.

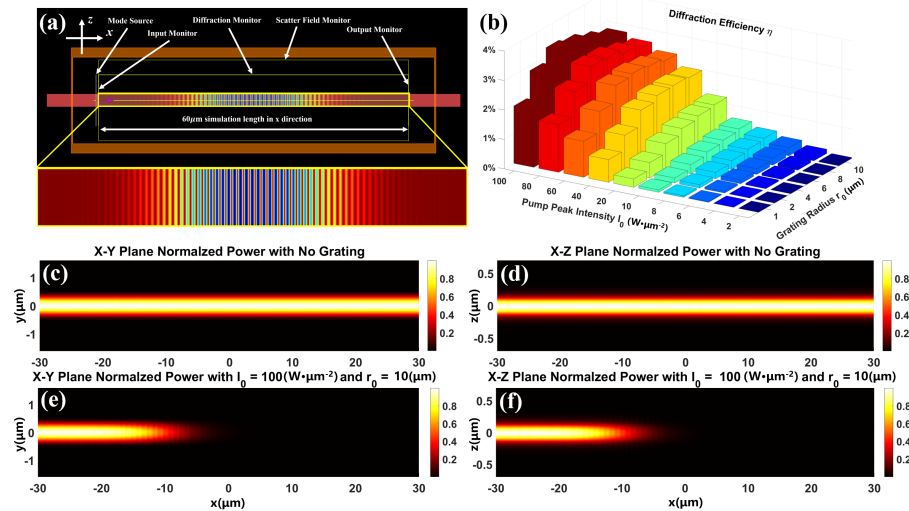


Fig. 5. (a) Illustration of FDTD simulation configuration, including necessary monitors and detailed nk map. (b) Diffraction transmittance with different pump sets, including pump peak intensity and grating radius. (c) Power Distribution in the X-Y plane and X-Z plane of no grating and $I_0 = 100 \text{ W} \cdot \mu\text{m}^{-2}$, $r_0 = 10 \mu\text{m}$ pump setting.

262 4.3. Results and Discussions

263 Fig. 5(b) illustrates the transmittance on the upper surface of the waveguide under the specified
 264 conditions. Due to the constant grating period, increasing the grating radius can enhance
 265 the number of stripes involved in diffraction. Therefore, it can be observed from the figure that
 266 under different light intensity conditions, there is a noticeable increase in transmittance when the
 267 pump light spot radius changes from $2 \mu\text{m}$ to $4 \mu\text{m}$. However, when the radius changes from
 268 $4 \mu\text{m}$ to $10 \mu\text{m}$, the increase in transmittance becomes less pronounced. In fact, at pump peak
 269 intensities exceeding $40 \text{ W} \cdot \mu\text{m}^{-2}$, increasing the radius beyond a certain threshold can lead to a
 270 reduction in transmittance. This is because the free carrier grating not only modulates the real
 271 part of the material's refractive index but also modulates the imaginary part of the refractive
 272 index. The absorption by free carriers reduces the energy of the probing light, resulting in
 273 decreased diffraction efficiency. With a comparison (Fig. (c)-(f)) between the power distribution

274 of no grating configuration and $I_0 = 100 \text{ W} \cdot \mu\text{m}^{-2}$, $r_0 = 10 \mu\text{m}$ pump setting configuration, it
 275 can be suggested that the power loss is not as a result of scattering from index variations. This
 276 suggests that the impact of increasing the number of stripes on diffraction efficiency is nonlinear
 277 and gradually diminishes as the radius of the free carrier grating increases. Beyond a certain
 278 threshold, increasing the number of stripes cannot offset the negative effects of free carrier
 279 absorption. This effect becomes more significant at higher pump light intensities.

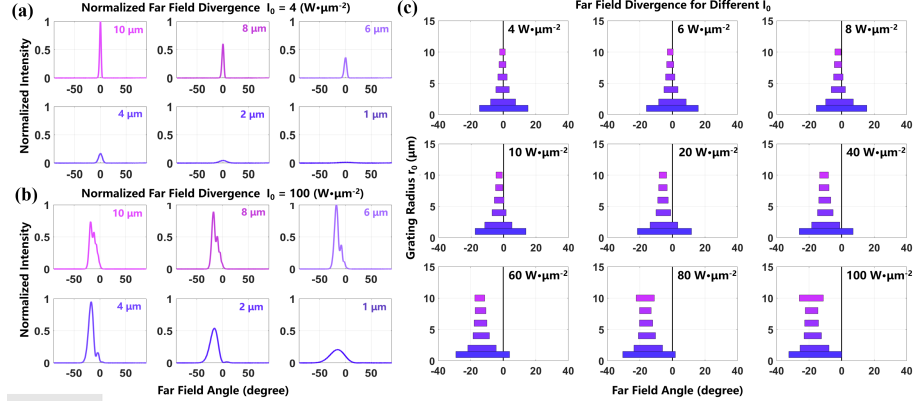


Fig. 6. (a) Illustration of carrier grating's far-field angular distribution under the pump with peak intensity $I_0 = 4 \text{ W} \cdot \mu\text{m}^{-2}$. (b) Illustration of carrier grating far-field angular distribution under the pump with peak intensity of $I_0 = 100 \text{ W} \cdot \mu\text{m}^{-2}$. (c) Illustration of half-width and direction of central peaks of the far field of different pump sets.

280 Fig. 6 displays the far-field analysis. Lumerical's far-field functionality enables the calculation
 281 of the superposition of the electromagnetic field on a spherical surface located 1 meter away
 282 from a specified monitor. Consequently, the far-field angular distribution on the upper surface of
 283 the waveguide can be computed. Fig. 6(a) presents the normalized far field distribution for a
 284 pump peak intensity of $4 \text{ W} \cdot \mu\text{m}^{-2}$ (i.e., the maximum values of the far field intensity data for
 285 the six radius settings are scaled to 1). As the radius increases, the far-field distribution gradually
 286 becomes more concentrated, and the central intensity significantly increases. However, in the
 287 case depicted in Fig. 6 (b) near the damage threshold of $100 \text{ W} \cdot \mu\text{m}^{-2}$, the far-field center shifts
 288 by approximately -18° , and as the radius increases, sidelobes with increasing intensity appear on
 289 the right side of the main beam, severely affecting the concentration of the far-field beam.

290 Fig. 6 (c) illustrates the influence of different radii on the far-field center and far-field
 291 divergence angle under a specific pump peak intensity. The horizontal position of the rectangle's
 292 center represents the direction of the maximum of the far field, the vertical position represents
 293 the corresponding radius of the carrier grating, and the length of the rectangle represents the
 294 half-angle width of the far field, with each black line displaying the vertical direction. As
 295 the pump intensity increases, the far field angle gradually shifts away from the center. When
 296 the intensity reaches $80 \text{ W} \cdot \mu\text{m}^{-2}$, increasing the radius leads to sidelobes and worsens the
 297 half-angle width. This implies that increasing both the intensity and the radius not only fails to
 298 enhance diffraction efficiency but also reduces the concentration of the far field beam, which has
 299 a detrimental effect on practical measurements.

300 The above results can be explained as the following analysis. As mentioned in section 3, the
 301 phase matching condition:

$$\frac{2\pi n_{eff}}{\lambda_{probe}} - \frac{2\pi}{\Lambda} = \frac{2\pi n_{cladding}}{\lambda_{probe}} \sin(\theta) \quad (7)$$

302 Under the configuration of vertical emission, the above equation's LHS should equal 0. However,
303 this pre-assumes n_{eff} is a constant. In fact, the carrier-induced FCI effect reduces the real part
304 of the refractive index, rendering n_{eff} decrease. Therefore, LHS is less than 0, which induces a
305 negative of θ in the RHS of the equation. To eliminate the shift from vertical emission, one should
306 increase Λ . Considering θ equals to -18° , $\Lambda' = [n_{eff} - n_{cladding} \sin(\theta)]/\lambda_{probe} \approx 0.6751\mu m$,
307 which is 20% greater than the origin one. And the pumping angle ϕ reduces from 45° to about
308 36° . Moreover, at a certain pump intensity, the radius increasing also leads to a slight shift of the
309 center direction at the far-field. This is because a higher grating radius causes a larger region of
310 low refractive index region, effectively reducing the n_{eff} of the mode.

311 The sidelobes caused by higher pump intensity are the result of truncated Gaussian envelopes
312 of the near field. Far-field distribution can be treated as the Fourier Transform of the near-field
313 distribution. In lower pump intensity, the field of the waveguide's upper surface is a periodical
314 field modulated by an entire Gaussian-shaped envelope, leading to a large main angle at the
315 far-field. However, the FCA effect induced by high pump intensity reduced mode intensity along
316 the x direction, truncating the field's Gaussian envelop with a fast decay at the right side of the
317 envelop's center, causing an unsymmetric near field which leads to sidelobes at the far field.

318 5. EXPERIMENT FEASIBILITY DISCUSSION

319 Based on the theoretical analysis of carrier dynamics and FDTD simulations of refractive index
320 distribution presented in the above sections, we can now discuss the feasibility of various
321 experimental approaches.

322 5.1. Choice of Pump

323 Firstly, let's consider the choice of laser source:

324 1. Nanosecond Pulse Laser or CW laser: Using nanosecond or continuous-wave lasers may
325 result in pump peak intensities that are too low. The maximum of refractive index change
326 induced by a nanosecond or continuous-wave pumping is less than 10^{-2} , leading to diffraction
327 efficiencies lower than -40 dB for the waveguide mode. This makes it difficult to distinguish
328 diffraction signals from scattered light introduced by waveguide surface roughness. However,
329 using continuous-wave light with ultra-small bandwidth for the pump in the SOI system may be
330 feasible if the pump is modulated. Lock-in amplification of the diffraction signal may help to
331 separate it from the scattered signal. This configuration is shown in Fig. 7(a).

332 2. Picosecond Pulse Laser: Picosecond lasers can achieve diffraction efficiencies exceeding
333 -20 dB. By appropriately increasing the radius of the free carrier grating and the pump intensity,
334 diffraction efficiency can be optimized. However, as discussed earlier, there are limitations
335 when the pump peak intensity on the waveguide surface exceeds $40 W \cdot \mu m^{-2}$. One concern is
336 the detrimental effect of increased free carrier absorption on diffraction efficiency, while the
337 other is the adverse impact of sidelobes on the concentration of the far-field beam, affecting the
338 measurement of diffraction signals. As shown in Fig. 7(b), If continuous-wave light is chosen as
339 the probe, higher temporal precision is required for the diffraction light detector. In this case, the
340 presence of the pulse laser is very short-lived, and the time window for the appearance of the
341 diffraction signal is on the picosecond timescale. A time resolution smaller than this timescale is
342 needed for accurate measurements. If pulsed light is chosen for probing, a delay setup is required
343 to interfere with the diffraction signal with a local probe signal using autocorrelation methods As
344 shown in Fig. 7(c). The advantage of this approach is that the time resolution requirements for
345 measurements can be reduced.

346 If a smaller pump radius is used or if the intensity is high, it can lead to an increase in the
347 half-width of the far-field main peak of the diffraction signal. This may result in the expansion of
348 the spatial distribution of intensity, necessitating refocusing of the diffraction signal. Otherwise,
349 the reduced power per unit area at the far field can pose challenges for detection. If near-field

350 diffraction signal reception is chosen, such as at the cladding surface, in this scenario, the
351 divergence area of the diffraction light is smaller, which is more favorable for signal detection.

352 *5.2. Control of Period Control*

353 Another important consideration in the experiment is the control of the carrier grating period.
354 For the mode of interest (e.g., TE mode, TM mode, or higher-order modes), the required grating
355 period can be calculated through phase matching.

356 1. If the waveguide has a cladding, to prevent power loss due to oblique incidence at the
357 interface and the appearance of higher-order diffraction signals, the emission direction can be
358 chosen to be perpendicular to the upper surface of the waveguide. According to the FDTD
359 simulation results, increasing the pump intensity can alter the emission direction. Experimenters
360 need to adjust the pumping angle based on specific simulation results to ensure that the center of
361 the far-field optical field is in the vertical direction.

362 2. If there is no cladding, further calculations are needed to determine the optimal emission
363 angle. This is because as the diffraction direction becomes smaller relative to the mode propagation
364 direction, the required grating period increases. Carriers need more time to move from one peak
365 to the nearest valley in the periodic distribution, resulting in a longer presence of the grating,
366 which increases the total diffraction energy. However, smaller angles introduce more diffraction
367 signal orders, which reduces the signal strength of the main order. The combined effects require
368 experimenters to simulate and determine using the methods discussed in this paper.

369 *5.3. Control of Carrier Grating Radius*

370 Since the high spatial resolution approach requires interference between two pump beams in a
371 spatial range on the order of $10 \mu\text{m}$, careful consideration is needed when adjusting the carrier
372 grating's radius. Commonly used spatial optical modules have apertures that are too large
373 compared to the working distance, limiting the possibility of focusing and interfering with two
374 beams of light in such a confined space. The use of two fiber lenses can achieve the desired
375 outcome (as shown in Fig. 8(d)). The Gaussian beam waist radius w_0 output by the conical fiber
376 lens is on the order of micrometers and can be controlled by adjusting the angle ψ and curvature
377 r_f of the top cone to control the beam waist radius w_0 and distance z_0 . If it is necessary to increase
378 the optical intensity in the waveguide width direction, one can also choose a wedge-shaped fiber
379 to output an elliptical beam, thereby reducing the beam radius in the y-direction and increasing
380 the pump power density. Moreover, using lensed fibers for near-field collection of the detection
381 light is also a feasible approach to consider. Additionally, if the spatial resolution of the spatial
382 light modulator is sufficiently small compared to the grating period, it can also be a viable option.

383 *5.4. Guideline*

384 Although the theoretical and simulation framework is based on the SOI system, the concept can be
385 extended to other similar on-chip systems. Firstly, it is necessary to determine the semiconductor
386 characteristics of the material used in the system detected. This includes parameters such as
387 bandgap width, optical absorption characteristics, carrier generation, recombination, diffusion
388 properties, as well as FCI and FCA parameters. Secondly, establish the damage threshold of
389 the material to avoid damaging the chip due to excessively high laser power. Thirdly, identify
390 the modes of interest for detection and perform grating period analysis. This technique involves
391 numerical calculations based on partial differential equations and FDTD simulations to determine
392 the pump intensity and carrier grating radius. These parameters are critical for optimizing
393 diffraction efficiency, and far-field beam divergence angle, with a need for high detection spatial
394 resolution.

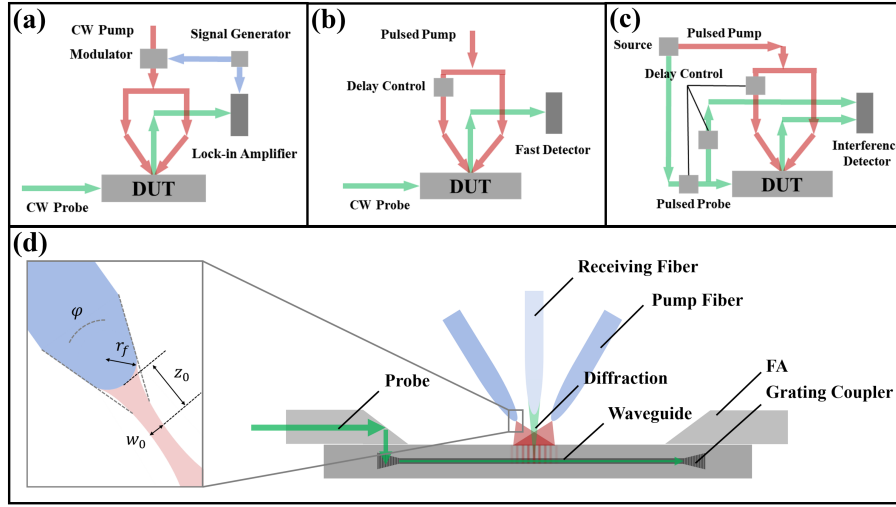


Fig. 7. (a) Configuration using CW form of pump. (b) Configuration using Pulsed form of pump and CW form of probe. (c) Configuration using Pulsed form of pump and Pulsed form of probe. (d) Illustration of a feasible experiment design using lensed fibers as pumping and receiving. The probe signal is injected into the chip by Fiber Arrays and Grating coupler, passing through the Device Under Test(DUT) and diffracting out by the carrier grating which is generated by the pump. The diffraction signal is received by a conical lensed fiber placed at a specific location. The pump is guided by two lens fibers aligned with a pre-designed angle.

395 6. Conclusion

396 This work provides a brief overview of the fundamental principles of TGS technology and
 397 its previous applications in silicon bulk materials and on-chip SOI systems. We proposed an
 398 integrated photonics chip detection scheme based on carrier grating and briefly analyzed the
 399 grating wavevectors, plasmonic effects, and damage thresholds in SOI strip waveguides. A carrier
 400 dynamics model is established, and numerical calculations are performed to assess the impact
 401 of different pump pulse widths on carrier recombination and diffusion in the SOI configuration
 402 within the range of damage threshold limitations. Leveraging the FCI and FCA effects based on
 403 carrier distribution, this work introduces refractive index distributions into FDTD simulations
 404 to compute carrier grating diffraction efficiency and far-field divergence characteristics under
 405 various parameter settings. The results indicate that above a certain carrier radius, the higher
 406 pump peak intensity induces negative effects on diffraction efficiency and far-field concentration
 407 as the grating radius increases. Finally, the feasibility of the experimental approach is discussed,
 408 along with specific construction approaches.

409 Funding.

410 Acknowledgments.

411 **Disclosures.** The authors declare no conflicts of interest.

412 Data Availability Statement.

413 References

- 414 1. C.-Y. Hsu, G.-Z. Yiu, and Y.-C. Chang, "Free-space applications of silicon photonics: A review," *Micromachines* **13**
 415 (2022).
- 416 2. C. Dhote, A. Singh, and S. Kumar, "Silicon photonics sensors for biophotonic applications—a review," *IEEE Sensors
 417 J.* **22**, 18228–18239 (2022).

- 418 3. J. Wang and Y. Long, "On-chip silicon photonic signaling and processing: a review," *Sci. Bull.* **63**, 1267–1310
419 (2018).
- 420 4. W. Bogaerts and L. Chrostowski, "Silicon photonics circuit design: Methods, tools and challenges," *Laser &*
421 *Photonics Rev.* **12**, 1700237 (2018).
- 422 5. X. Mu, S. Wu, L. Cheng, and H. Fu, "Edge couplers in silicon photonic integrated circuits: A review," *Appl. Sci.* **10**
423 (2020).
- 424 6. L. Cheng, S. Mao, Z. Li, *et al.*, "Grating couplers on silicon photonics: Design principles, emerging trends and
425 practical issues," *Micromachines* **11** (2020).
- 426 7. T. Sjodin, C.-M. Li, H. Petek, and H.-L. Dai, "Ultrafast transient grating scattering studies of carrier dynamics at a
427 silicon surface," *Chem. Phys.* **251**, 205–213 (2000).
- 428 8. F. Hofmann, M. P. Short, and C. A. Dennett, "Transient grating spectroscopy: An ultrarapid, nondestructive materials
429 evaluation technique," *MRS Bull.* **44**, 392–402 (2019).
- 430 9. U. Choudhry, T. Kim, M. Adams, *et al.*, "Tutorial: Characterizing microscale energy transport in materials with
431 transient grating spectroscopy," (2021).
- 432 10. M. Borghi, C. Castellan, S. Signorini, *et al.*, "Nonlinear silicon photonics," *J. Opt.* **19**, 093002 (2017).
- 433 11. T. Sjodin, H. Petek, and H.-L. Dai, "Ultrafast carrier dynamics in silicon: A two-color transient reflection grating
434 study on a (111) surface," *Phys. Rev. Lett.* **81**, 5664–5667 (1998).
- 435 12. R. Bruck, B. Mills, B. Troia, *et al.*, "Device-level characterization of the flow of light in integrated photonic circuits
436 using ultrafast photomodulation spectroscopy," *Nat. Photon* **9**, 54–60 (2015).
- 437 13. R. Bruck, B. Mills, D. J. Thomson, *et al.*, "Picosecond optically reconfigurable filters exploiting full free spectral
438 range tuning of single ring and vernier effect resonators," *Opt. Express* **23**, 12468–12477 (2015).
- 439 14. R. Bruck, K. Vynck, P. Lalanne, *et al.*, "All-optical spatial light modulator for reconfigurable silicon photonic circuits,"
440 *Optica* **3**, 396–402 (2016).
- 441 15. A. Molina, I. Aldaya, J. Pita Ruiz, *et al.*, "Optical free-carrier generation in silicon nano-waveguides at 1550 nm,"
442 *Appl. Phys. Lett.* **112**, 251104 (2018).
- 443 16. K. Sokolowski-Tinten and D. von der Linde, "Generation of dense electron-hole plasmas in silicon," *Phys. Rev. B* **61**,
444 2643–2650 (2000).
- 445 17. I. Aldaya, A. Gil-Molina, J. L. Pita, *et al.*, "Nonlinear carrier dynamics in silicon nano-waveguides," *Optica* **4**,
446 1219–1227 (2017).
- 447 18. P. S. Goley, E. Preisler, and J. D. Cressler, "Localized excitation of silicon photonic waveguides for measurement of
448 free-carrier lifetime and surface recombination velocity," in *2021 Conference on Lasers and Electro-Optics (CLEO)*,
449 (2021), pp. 1–2.
- 450 19. F. M. H. Jichler, "Diffraction efficiency and decay times of free-carrier gratings in silicon," *J. Appl. Phys.* **53**,
451 3237–3242 (1982).
- 452 20. A. Singh, "Free charge carrier induced refractive index modulation of crystalline silicon," in *7th IEEE International
453 Conference on Group IV Photonics*, (2010), pp. 102–104.
- 454 21. R. Soref and B. Bennett, "Electrooptical effects in silicon," *IEEE J. Quantum Electron.* **23**, 123–129 (1987).
- 455 22. X. Wang, Z. Shen, and X. Ni, "Laser-induced damage threshold of silicon in millisecond, nanosecond, and picosecond
456 regimes," *J. Appl. Phys.* **108**, 033103 – 033103 (2010).
- 457 23. D. Marcuse, "Light scattering from periodic refractive-index fluctuations in asymmetric slab waveguides," *IEEE J.
458 Quantum Electron.* **11**, 162–168 (1975).
- 459 24. R. Bonilla and P. Wilshaw, "On the c-si/sio 2 interface recombination parameters from photo-conductance decay
460 measurements," *J. Appl. Phys.* **121**, 135301 (2017).
- 461 25. M. Born and E. Wolf, *Principles of Optics* (1980).
- 462 26. H. J. Eichler, P. Günter, and D. W. Pohl, *Laser-Induced Gratings* (1986).